Available online at www.sciencedirect.com
SciVerse ScienceDirect
Scripta Materialia 68 (2013) 885–888
Scripta MATERIALIA
www.elsevier.com/locate/scriptamat

Elevated-temperature impact toughness of Mg–(Gd, Y)–Zr alloy

Y.L. Mu,[a] Q.D. Wang,[a,*] M.L. Hu,[a] V. Janik[b] and D.D. Yin[a]

[a]*National Engineering Research Center of Light Alloy Net Forming, State Key Laboratory of Metal Matrix Composites, Shanghai Jiao Tong University , Dongchuan Road 800, Shanghai 200240, China*
[b]*Czech Technical University in Prague, Karlovo nam. 13, Prague 12135, Czech Republic*

Received 18 December 2012; revised 8 February 2013; accepted 9 February 2013
Available online 21 February 2013

The Charpy impact results for Mg–10Gd–3Y–0.5Zr and Mg–11Y–5Gd–2Zn–0.5Zr alloys at various temperatures showed that Mg–10Gd–3Y–0.5Zr was more sensitive to temperature. The increase in impact toughness with temperature was related to the blunt crack-tip at high temperatures. The delamination and local melt of matrix were responsible for the brittle-to-ductile transition of GW103 alloy. The branch and bridging of cracks resulting from ordered phases played an import role in the change in fracture mode from cleavage fracture to quasi-cleavage and dimple-fracture for WGZ1152 alloy.

Keywords: Magnesium alloys; Toughness; Impact behaviour; Fracture; Long-period stacking ordered

It has been demonstrated that magnesium (Mg) alloys containing gadolinium (Gd) and yttrium (Y) possess high strength [1–4], creep-resistance [5–7] and wear-resistance [8,9]. These alloys thus have great potential to be used as heat-resistant alloys in the automotive and aerospace industries. However, most research has focused on the static mechanistic behavior of Mg alloys. When the materials are subjected to impulsive loads such as impact, explosion or thermomechanical shock during service, the dynamic response and fracture process exhibits special characteristics that differ from those of static response, owing to the presence of high loading rates. Therefore, it is necessary for a proper assessment of the dynamic fracture behavior of Mg–(Gd, Y) alloys for structural applications, especially at elevated temperatures. One method is to investigate their impact toughness at various temperatures. There have been many studies on the fracture toughness of wrought Mg/Mg alloy at room temperature [10–16]. Recently, Liao et al. [17,18] reported the room temperature impact toughness of extrude Mg alloy. Results demonstrated that the room temperature fracture/impact toughness of wrought Mg/Mg alloy is affected by microstructural features, such as texture [10,11], solid-solution/precipitation strengthening [12–15], grain size [13,16–19] and oxygen content [17]. However, few reports focus on the elevated-temperature impact toughness of cast heat-resistant Mg–RE alloy, which is important for estimating the service performance of Mg–RE alloy under high temperature and transient dynamic load conditions. However, it is difficult to obtain more details near the crack tips throughout the test process, owing to the extremely short impact time.

In the present work, the impact toughness and fracture feature of two heat-resistant Mg–RE alloys, peak-aged Mg–10Gd–3Y–0.5Zr (wt.%) (GW103) and Mg–11Y–5Gd–2Zn–0.5Zr (wt.%) (WGZ1152), were studied at a temperature range from room temperature to 350 °C. It needs to be emphasized that the local stress states of impact samples are quite different from the plane-strain fracture toughness test. The impact load and impact energy, therefore, cannot truly reflect the critical stress-intensity factor K_{Ic} of samples. The impact toughness represents the whole energy consumption of the specimen from elastic deformation to crack initiation until fracture, while K_{Ic} reflects the energy consumption before unstable extension of the crack. However, the results still have reference value for assessing the elevated-temperature fracture responses under impact loading.

GW103 alloy and WGZ1152 alloy were prepared from high purity (≥99.9 wt.%) Mg, Zn and master alloys of Mg–25 wt.% Gd, Mg–25 wt.% Y and Mg–30 wt.% Zr. Further details are available in Refs. [2–4,6]. The GW103 alloy was solution heat-treated at

* Corresponding author. Tel.: +86 21 54742715; fax: +86 21 34202794; e-mail: wangqudong@sjtu.edu.cn

1359-6462/$ - see front matter © 2013 Acta Materialia Inc. Published by Elsevier Ltd. All rights reserved.
http://dx.doi.org/10.1016/j.scriptamat.2013.02.031

500 °C for 6 h and quenched in water. The T6 peak-aging heat treatment involved aging in a hot oil-bath at 225 °C for 16 h followed by air cooling. The WGZ1152 alloy was solution treated at 535 °C for 20 h, quenched in water at 25 °C, and then aged at 225 °C for 24 h in an oil-bath. All the impact tests were performed on material that had undergone the peak-aged (T6) heat treatment.

Impact toughness was determined in terms of the Charpy impact testing instrument IMP450J at temperatures ranging from room temperature (RT) to 350 °C to record the load and displacement of the hammer. The specimens for the impact test were Charpy unnotched test specimens with dimensions $10 \times 10 \times 55$ mm. All specimens were heated to the testing temperature and held for 20 min. An average of three measurements were used to evaluate the impact toughness. Scanning electron microscopy (SEM; JEOL JSM-5200) was employed for observation of the fractured surface.

The microstructures of peak-aged GW103 and WGZ1152 alloy have been described previously [2–4]. The peak-aged microstructure evolution of GW103 alloy involves mainly α-Mg solid solution, fine and dense rod-like β' precipitates inside α-Mg matrix. The average equiaxed α-phase grain size of the peak-aged alloy was ~40 μm. The peak-aged WGZ1152 alloy consists mainly of a fine-lamellar long-period stacking ordered (LPSO) structure distributed in the grain interior, strip-shaped LPSO $Mg_{12}YZn$ distributed along the grain boundaries, dense spheroidal β' precipitates and the α-Mg solid solution. The average grain size of WGZ1152 alloy was ~120 μm. In addition, Gd/Y enriched cuboidal phase (face-centered cubic) and Zr cores exist in both alloys.

Typical impact load–displacement (LD) curves and impact energy (IE) curves (insets) at RT and 350 °C for both alloys are shown in Figure 1a and b. The LD curve for GW103 alloy can be divided into three phases at RT: the elastic phase (I), the hardening phase (II) and the collapse phase (III). Here, the absorbed IE during phases I and II includes crack initiation and growth energy, while phase III represents crack instability propagation energy. The LD curve for WGZ1152 alloy, however, shows a distinct peak and the absence of phase II, indicating the rapid extension of the crack the moment the crack initiates under impact loading. It is clear that the crack initiation and growth energy is much greater than the crack instability propagation energy for GW103 alloy, demonstrating higher ductility and fracture resistance (toughness) than the WGZ1152 alloy. As shown in Figure 1b, the most apparent difference for impact response at temperatures up to 350 °C is the much higher displacement and total IE (inset) for both alloys, which increases by 300–400% compared with that of RT (Fig. 1a). However, it should be noted that not only does the impact load decrease for both alloys, but notable changes at phase II of LD curves have occurred. First, a hardening phase appeared on the WGZ1152 LD curve, while phase II of GW103 LD curve can be subdivided into a sustained load rise zone (II_1) and a constant load zone (II_2). Second, the load in phase II for WGZ1152 alloy is greater.

Figure 2a and b shows the impact LD curves of GW103 and WGZ1152 alloy at RT of 100, 150, 200, 250, 300 and 350 °C, respectively. The maximum load for GW103 alloy decreases gradually from 10 kN at RT to 5.5 kN at 350 °C, but ranges between 7 and

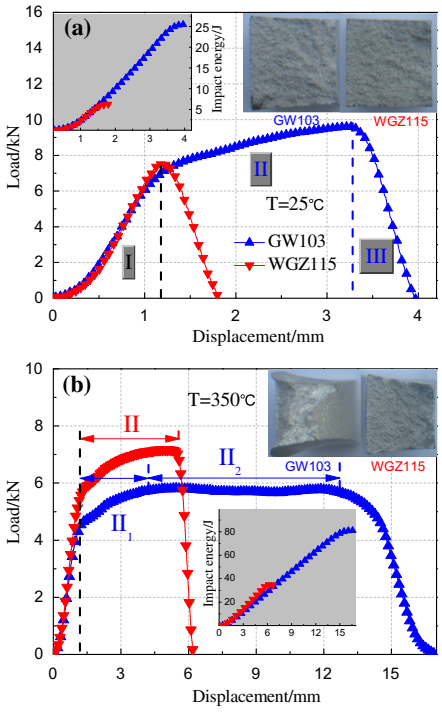

Figure 1. Typical Charpy unnotched impact load and energy vs. displacement curves of GW103 alloy and WGZ1152 alloy at (a) room temperature and (b) 350 °C. Macro-fractographs of GW103 alloy and WGZ1152 alloy impact at RT and 350 °C (insets).

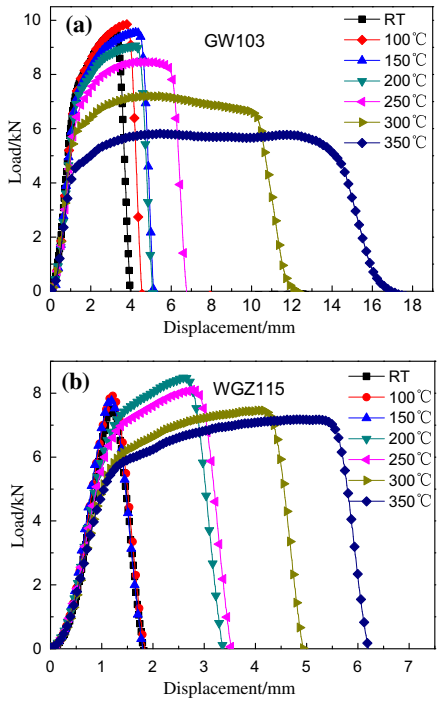

Figure 2. LD curves for (a) GW103 and (b) WGZ1152 at various temperatures.

9 kN for WGZ1152 alloy. At temperatures >250 °C, the maximum load for WGZ1152 alloy exceeds that for GW103 alloy, but the value of total energy for GW103 alloy is still higher, owing to the longer impact displacement. For WGZ1152 alloy, the values of load in phase I are progressively lower with increasing temperature. However, phase II, whose max load value is higher than phase I, appears at 200 °C and above. The UTS of WGZ1152 alloy at elevated temperatures has shown a similar response [4]. The mechanism of this unusual phenomenon, however, remains enigmatic.

The IE as a function of temperature is shown in Figure 3a. The total IE for both alloys increases with test temperature, indicating rising impact toughness at high temperatures. It seems that the impact toughness of GW103 alloy is much more sensitive to impact temperature, because the amount of IE increases (from 24 J at RT to 82 J at 350 °C) per 100 °C (E_{100}) reaches ~17 J, but E_{100} reduces to ~8 J for WGZ1152 alloy (from 6 J at RT to 32 J at 350 °C). The rapid rise in total IE and appreciable reduction in load as the impact temperature exceeds 200 °C are essential features of elevated-temperature impact response for both alloys. It should be remarked here that the increase in IE comes mainly from phase II of the LD curve (Fig. 2a and b), that is, the crack initiation and growth process. Figure 3b shows the relation between the ultimate tensile strength (UTS) [3,4] and IE of both alloys at various temperatures. GW103 alloy shows an improved combination of strength and impact toughness compared with WGZ1152 alloy. The temperature dependence of tensile properties of GW103 and WGZ1152 alloys has demonstrated that UTS and elongation for GW103 alloy were higher than that for WGZ1152 alloy at 200 °C and below, while UTS and elongation were lower for GW103 alloy than for WGZ1152 alloy >200 °C [3,4]. In addition, the grain size [16,17–19] may be one of the reasons for higher impact toughness for GW103 alloy (~40 μm) than WGZ1152 alloy (~120 μm), indicating that it is possible to attain higher strength and impact toughness at high temperatures for WGZ1152 alloy by grain refinement.

The macro-fractographs and micro-fractographs of both alloys samples impacted at temperatures between RT and 350 °C are shown in Figure 1 (insets) and Figure 4, respectively. It is clear that both alloys fail in brittle transgranular mode at RT. The shear lips are barely noticeable on the fracture surface, and apparent radial marks cover the whole fracture surface. Low-energy decohesion, without visible plastic deformation and evident secondary cracks on the micro-fractographs of both alloys shown in Figure 4a and b also identify the mechanism of formation of RT brittle fracture on the macroscopic scale. These observations are in accordance with the LD response of both alloys with relative apparent peak load (P) at low impact temperature (≤150 °C), which indicates that the crack propagates rapidly under the impact load once it originates. As the impact temperature reaches 350 °C, the quite narrow shear lips on the sides of the fracture surface of WGZ1152 specimen can be observed, although the radiation zone still covers most of the surface. For GW103 alloy, the fibrous zone and shear rupture zone of the specimen impacted at 350 °C cover the whole surface, indicating considerable plastic deformation. Moreover, the GW103 specimens exhibited minor delaminations, where cracks branched

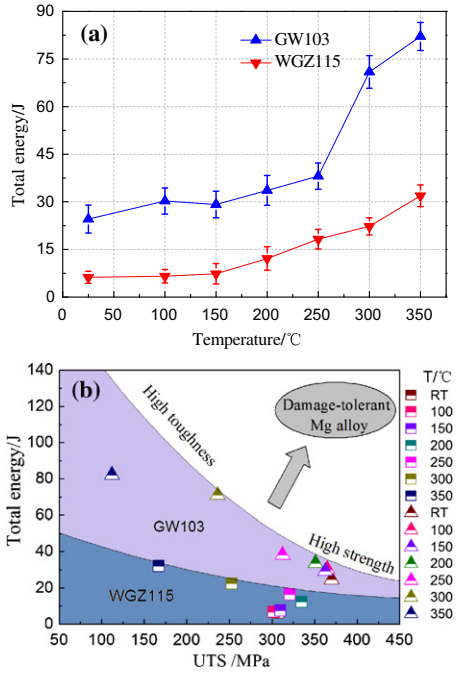

Figure 3. IE absorption of GW103 and WGZ1152 alloy as a function of (a) temperature and (b) UTS [3,4] in the temperature range from room temperature to 350 °C.

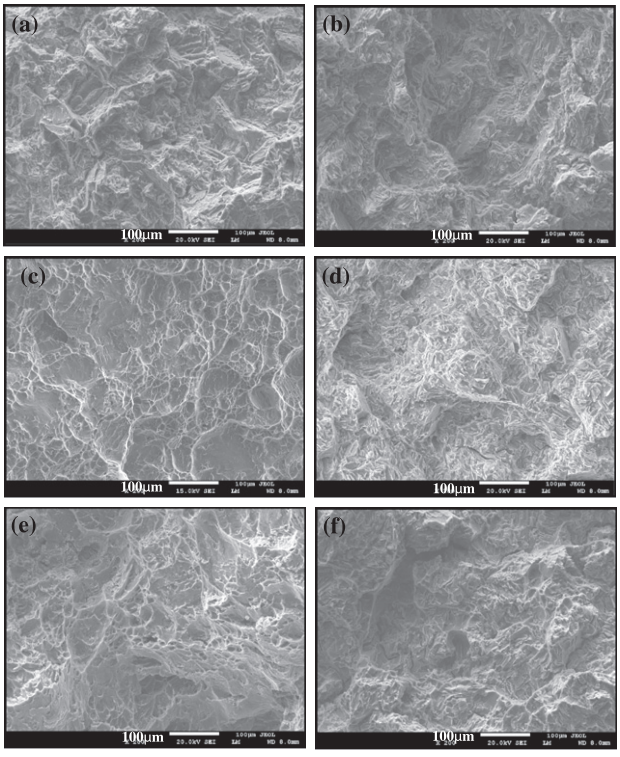

Figure 4. Micro-fractographs of samples impact for GW103 alloy at: (a) room temperature; (c) 250 °C; (e) 350 °C; and for WGZ1152 alloy at: (b) room temperature; (d) 250 °C; (f) 350 °C.

parallel to the longitudinal direction of the impact test bar, and therefore the crack propagation in the striking direction were substantially blunted.

The brittle-to-ductile transition occurred clearly for GW103 alloy with rising impact temperature. The features of fracture surface morphology of the alloy changed from cleavage steps (Fig. 4a) to dimples (Fig. 4c) when the impact temperature increased from RT to 250 °C. The dimples' nucleation, growth and coalescence are the major fracture mechanisms, and the samples can absorb more energy during the impact fracture process at a temperature of 250 °C. As the impact temperature reached 350 °C, tear ridges and widespread viscous-like flow shear surface in the α-Mg solid solution (Fig. 4e) could be observed. The local detail of viscous-like flow shear surface, a ripple morphology, shown in Figure 4e indicates that local melt may occur for GW103 alloy under elevated-temperature impact load, which can explain the cause of much greater crack extension phase (phase II) and IE at 350 °C than that at 250 °C in Figures 2a and 3. The higher impact toughness for GW103 alloy as the impact temperature exceeds 250 °C can therefore be attributed to three factors: (I) the plastic zone size of the crack-tip increases as a result of decreasing yield strength at high temperatures, leading to a blunt crack front to improve intrinsic toughening; (II) the minor delamination relaxes triaxial stress conditions ahead of the crack-tip and blunts the crack-tip, thus improving the impact toughness [20]; (III) crack-tip blunting/shielding due to local melt of the matrix.

A more detailed observation of the fracture surface of WGZ1152 alloy at 350 °C (Fig. 4f) shows the change in fracture mode from cleavage fracture to quasi-cleavage and dimple fracture for WGZ1152 alloy, indicating weak energy dissipation ability over the whole range of impact temperature, corresponding to the similar value of P at various temperatures and low E_{100} in Figures 2b and 3a. One prominent feature for WGZ1152 alloy at the high impact temperature is the rising load during the hardening phase (Fig. 2b). The feature resulting from thermally stable LPSO phases strengthening [5] elevated the stress level at the crack-tip, which enhanced the driving force of crack propagation, thus reducing the impact toughness. The other prominent feature manifests mainly as more secondary cracks on the fracture surface (Fig. 4f), resulting from the branch and bridging of cracks, improving the impact toughness. It should be mentioned that the crack-tip blunting due to large plastic zone size at high temperatures has also played an import role in improvement of the impact toughness of WGZ1152 alloy in addition to the branch and bridging of cracks. This can be confirmed from the plastic deformation of α-Mg matrix in Figure 4f. At low impact temperatures, the cleavage faces and steps form rapidly once the fracture stress of brittle α-Mg or LPSO phase along the grain boundaries is reached by stress concentration. Larger and more cleavage faces can thus be observed on the fracture surface (Fig. 4b). With the rising impact temperature, the yield strength of α-Mg matrix decreases, and even the brittle LPSO phases themselves have a certain capacity for plastic deformation, alleviating the stress concentration near the brittle phase. The growth of the initial micro-crack on the brittle phase becomes slow, which creates favorable conditions for the initiation of a lot of micro-crack on other positions, further reducing the stress concentration. Therefore, the secondary cracks on the fracture surface for WGZ1152 alloy multiplied at high impact temperatures.

The effect of temperature on the impact response and fractography was evaluated in GW103 and WGZ1152 alloys. It was found that GW103 alloy exhibited higher impact toughness than WGZ1152 alloy. The total IE for both alloys rose remarkably as the impact temperature increased, owing to the enhanced dynamic plastic deformation ability. Delamination and local melt of matrix under elevated-temperature impact load led to the brittle-to-ductile transition of GW103 alloy. The increase in branches and bridging of cracks resulting from LPSO phases plays an import role in improving the impact toughness of WGZ1152 alloy.

The authors gratefully acknowledge financial support from the National Natural Science Foundation of China (No. 51074106), the Key Hi-Tech Research and Development Program of China (2009AA033501) and the National Key Technology R&D Program of China (2011BAE22B01-5, 2006BAE04B01-2).

[1] I.A. Anyanwu, S. Kamado, Y. Kojima, Mater. Trans. 42 (2001) 1206.
[2] S.M. He, X.Q. Zeng, L.M. Peng, X. Gao, J.F. Nie, W.J. Ding, J. Alloys Comp. 427 (2007) 316.
[3] V. Janik, D.D. Yin, Q.D. Wang, S.M. He, C.J. Chen, Z. Chen, C.J. Boehlert, Mater. Sci. Eng. A 528 (2011) 3105.
[4] D.D. Yin, Q.D. Wang, Y. Gao, C.J. Chen, J. Zheng, J. Alloys Comp. 509 (2011) 1696.
[5] I.A. Anyanwu, S. Kamado, Y. Kojima, Metall. Mater. Trans. A 42 (2001) 1212.
[6] D.D. Yin, Q.D. Wang, C.J. Boehlert, V. Janik, Metall. Mater. Trans. A 43 (2012) 3338.
[7] X.B. Liu, X. Guan, R.S. Chen, E.H. Han, Trans. Nonferrous Met. Soc. China 20 (2010) S545.
[8] M.L. Hu, Q.D. Wang, C. Li, W.J. Ding, Trans. Nonferrous Met. Soc. China 22 (2012) 1918.
[9] M.L. Hu, Q.D. Wang, C.J. Chen, D.D. Yin, W.J. Ding, Z.S. Ji, Mater. Design 42 (2012) 223.
[10] H. Somekawa, T. Mukai, Mater. Sci. Eng. A 459 (2007) 366.
[11] H. Somekawa, T. Mukai, Scr. Mater. 53 (2005) 541.
[12] H. Somekawa, Y. Osawa, A. Singh, T. Mukai, J. Mater. Res. 23 (2008) 1128.
[13] H. Somekawa, A. Singh, T. Mukai, Scr. Mater. 56 (2007) 1091.
[14] H. Somekawa, A. Singh, T. Mukai, J. Mater. Res. 22 (2007) 965.
[15] H. Somekawa, Y. Osawa, T. Mukai, Scr. Mater. 55 (2006) 593.
[16] H. Somekawa, T. Mukai, Scr. Mater. 53 (2005) 1059.
[17] J.S. Liao, M. Hotta, A. Koshi, Mater. Lett. 65 (2011) 2995.
[18] J.S. Liao, M. Hotta, K. Kaneko, K. Kondoh, Scr. Mater. 61 (2009) 208.
[19] A. Ma, K. Suzuki, Y. Nishida, N. Saito, I. Shigematsu, M. Takagi, H. Iwata, A. Watazu, T. Imura, Acta Mater. 53 (2005) 211.
[20] D.W. Kum, T. Oyama, J. Wadsworth, O.D. Sherby, J. Mech. Phys. 31 (1983) 173.